

Microwave imaging of a partially immersed non-uniform conducting cylinder

Wei Chien^{a,*}, Chien-Ching Chiu^b, Ching-Lieh Li^b and Chi-Hsien Sun^b

^a*Electronic Engineering Department, De Lin Institute of Technology, Taipei, Taiwan, China*

^b*Electrical Engineering Department, Tamkang University, Tamsui, Taiwan, China*

Abstract. In this paper, we investigate the imaging problem to determine both the shape and the conductivity of a partially immersed non-uniform conducting cylinder from the knowledge of scattered far-field pattern of TM waves by solving the ill-posed nonlinear equation. Based on the boundary condition and the measured scattered field, a set of nonlinear integral equations is derived and the inverse problem is reformulated into an optimization one. The steady-state genetic algorithm is then employed to find out the global extreme solution of the object function. As a result, the shape and the conductivity of the conductor can be obtained. Numerical results are given to demonstrate that even in the presence of noise, good reconstruction can be obtained.

Keywords: Inverse problem, partially immersed, non-uniform conducting cylinder, steady-state genetic algorithm

1. Introduction

In recent decades, the scientific community has addressed a growing interest to the detection and imaging of unknown objects located in inaccessible domains through the use of electromagnetic fields at microwave frequencies. As a matter of fact, the propagation of electromagnetic wave in the microwave range is significantly affected by the characteristics of the medium. Therefore, it is profitable to exploit such a phenomenon in order to sense an unknown scenario in a non-invasive fashion. Towards this end, several researches have been pursued in the framework of non-destructive evaluation and testing and biomedical diagnostics [1–11].

In general, inverse scattering problem is nonlinear and ill-posed due to lack of enough information from the measured scattering data [12]. During the imaging process, a large amount of parameters need to be retrieved from a limited number of independent measurements. Nonlinearity is another difficulty. The inverse scattering problem is nonlinear in nature because it involves the product of two unknowns, i.e., the electrical properties of object and the electric field within the object. And it can be solved by means of iterative optimization algorithm.

Recently, many methods have been proposed to reconstruct the shape of a 2-D perfect conductor cylinder, which can be classified into two catalogs, in general. The first is based on gradient searching scheme such as the Newton-Kantorovitch method [13,14], the Levenberg-Marguart algorithm [15, 16] and the successive-over-relaxation method [17]. However, for a gradient-based method, it is well

*Corresponding author: Wei Chien, Electronic Engineering Department, De Lin Institute of Technology, Tucheng City, Taipei County, Taiwan 23656, China. E-mail: chiu@ee.tku.edu.tw.

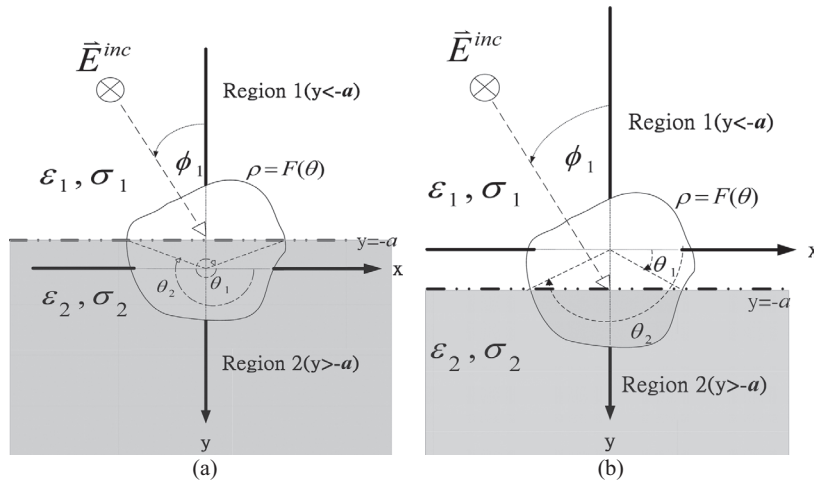


Fig. 1. (a) Geometry of the problem in (x, y) plane for the case $a > 0$. (b) Geometry of the problem in (x, y) plane for the case $a < 0$.

known that the convergence of the iteration depends highly on the initial guess. If a good initial guess is given, the speed of convergence can be very fast. On the other hand, if the initial guess is far away from the exact one, the searching tends to get fail [18]. In contrast, the second approach is population-based evolutionary algorithm, such as genetic algorithm [19–27], particle swarm optimization [28–33] and differential evolution algorithm [32–39]. These evolutionary algorithms are proposed to search the global extreme of the inverse problem to overcome the drawback of the deterministic methods. Based on stochastic strategies, these algorithms offer advantages relative to local inversion algorithms including strong search ability, simplicity, robustness, and insensitivity to ill-posedness. Chiu [40] first applied GA for the inversion of a buried imperfect conducting cylinder with the geometry described by a Fourier series (surface reconstruction approach). Moreover, Chiu [20] point out that the inverse problem by using SSGA is much better than SGA in time costing. The main advantage of Fourier series expansion is that for complicated shape, such as highly concave, the expansion is efficient if the center of unknown object is adequate.

In this paper, the scattering object is not immersed in a single medium, but is located right at the interface of two mediums instead, for which the theoretical and numerical analysis of the scattering problem become much more difficult. One has to deal with not only the usual target surface boundary condition, but also the media interface boundary condition. To the best of our knowledge, there are no investigations on the electromagnetic imaging of partially immersed non-uniform conducting cylinder. In this paper, the electromagnetic imaging of a partially immersed non-uniform conducting cylinder is first reported using SSGA. In Section 2, the relevant theory and formulation are presented. In Section 3, the details of the improved SSGA are given. Numerical results of reconstructed objects of different shapes and conductivities are shown in Section 4. Finally, some conclusions are drawn in Section 5.

2. Theoretical formulation

An imperfectly conducting cylinder with conductivity profile $\sigma(\theta)$ is partially immersed in a lossy homogeneous half-space, as shown in Figs 1(a) and (b). Media in Regions 1 and 2 are characterized by

permittivities and conductivities $(\varepsilon_1, \sigma_1)$ and $(\varepsilon_2, \sigma_2)$, respectively. The non-uniform conducting cylinder is illuminated by a transverse magnetic (TM) plane wave. The cylinder is of infinite extent in the z direction, and its cross-section is described in polar coordinates in the x, y plane by the relation $\rho = F(\theta)$, and the objects concerned are of star-like shape. We assume that the time dependence of the incident field is harmonic with factor $\exp(j\omega t)$. Let E^{inc} denote the incident E field from Region 1 with incident angle ϕ_1 . Owing to the interface between Regions 1 and 2, the incident plane wave generates two waves that would exist in the absence of the conducting object. Thus, the unperturbed fields are given by

$$E^i(x, y) = \begin{cases} E_1^i(x, y) = e^{-jk_1(x \sin \phi_1 + (y+a) \cos \phi_1)} + R e^{-jk_1(x \sin \phi_1 - (y+a) \cos \phi_1)}, & y \leq -a \\ E_2^i(x, y) = T e^{-jk_2(x \sin \phi_2 + (y+a) \cos \phi_2)}, & y > -a \end{cases} \quad (1)$$

where $R = \frac{1-n}{1+n}$, $T = \frac{2}{1+n}$, $n = \frac{\cos \phi_2}{\cos \phi_1} \sqrt{\frac{\varepsilon_2 - j\sigma_2(\theta)/\omega}{\varepsilon_1 - j\sigma_1(\theta)/\omega}}$

$$k_i^2 = \omega^2 \varepsilon_i \mu_0 - j\omega \mu_0 \sigma_i(\theta), \text{Im}(k_i) \leq 0, k_1 \sin \phi_1 = k_2 \sin \phi_2, i = 1, 2$$

Since the cylinder is partially immersed, the equivalent currents exist both in the upper half space and the lower half space. As a result, the details of Green's function are given first as follows:

- (1) When the equivalent current exists in the upper half space, the Green's function for the line source in the Region 1 can be expressed as

$$G_1(x, y; x', y') = \begin{cases} G_{21}(x, y; x', y'), & y > -a \\ G_{11}(x, y; x', y') = G_{f11}(x, y; x', y') + G_{s11}(x, y; x', y'), & y \leq -a \end{cases} \quad (2)$$

where

$$G_{21}(x, y; x', y') = \frac{1}{2\pi} \int_{-\infty}^{\infty} \frac{j}{\gamma_1 + \gamma_2} e^{-j\gamma_2(y+a)} e^{j\gamma_1(y'+a)} e^{-j\alpha(x-x')} d\alpha \quad (2.1)$$

$$G_{f11}(x, y; x', y') = \frac{j}{4} H_0^{(2)} \left[k_1 \sqrt{(x-x')^2 + (y-y')^2} \right] \quad (2.2)$$

$$G_{s11}(x, y; x', y') = \frac{1}{2\pi} \int_{-\infty}^{\infty} \frac{j}{2\gamma_1} \left(\frac{\gamma_1 - \gamma_2}{\gamma_1 + \gamma_2} \right) e^{j\gamma_1(y+2a+y')} e^{-j\alpha(x-x')} d\alpha \quad (2.3)$$

$$\gamma_i^2 = k_i^2 - \alpha^2, i = 1, 2, \text{Im}(\gamma_i) \leq 0, y' < -a$$

- (2) When the equivalent current exists in the lower half space, the Green's function for the line source in the Region 2 is given by

$$G_2(x, y; x', y') = \begin{cases} G_{12}(x, y; x', y'), & y \leq -a \\ G_{22}(x, y; x', y') = G_{f22}(x, y; x', y') + G_{s22}(x, y; x', y'), & y > -a \end{cases} \quad (3)$$

where

$$G_{12}(x, y; x', y') = \frac{1}{2\pi} \int_{-\infty}^{\infty} \frac{j}{\gamma_1 + \gamma_2} e^{j\gamma_1(y+a)} e^{-j\gamma_2(y'+a)} e^{-j\alpha(x-x')} d\alpha \quad (3.1)$$

$$G_{f22}(x, y; x', y') = \frac{j}{4} H_0^{(2)} \left[k_2 \sqrt{(x-x')^2 + (y-y')^2} \right] \quad (3.2)$$

$$G_{s22}(x, y; x', y') = \frac{1}{2\pi} \int_{-\infty}^{\infty} \frac{j}{2\gamma_2} \left(\frac{\gamma_2 - \gamma_1}{\gamma_2 + \gamma_1} \right) e^{-j\gamma_2(y+y'+2a)} e^{-j\alpha(x-x')} d\alpha \quad (3.3)$$

$$\gamma_i^2 = k_i^2 - \alpha^2, i = 1, 2, \text{Im}(\gamma_i) \leq 0, y' > -a$$

For programming purposes, the scattered field can be reformulated according to the following two cases:

[case1] if $a > 0$ ($\theta_1 > \theta_2$), as shown in Fig. 1(a)

$$E^S(\vec{r}) = \begin{cases} E_1^S(\vec{r}) = - \int_{\theta_1-2\pi}^{\theta_2} G_{12}(\vec{r}, F(\theta'), \theta') J(\theta') d\theta' \\ \quad - \int_{\theta_2}^{\theta_1} G_{11}(\vec{r}, F(\theta'), \theta') J(\theta') d\theta', & y \leq -a \\ E_2^S(\vec{r}) = - \int_{\theta_1-2\pi}^{\theta_2} G_{22}(\vec{r}, F(\theta'), \theta') J(\theta') d\theta' \\ \quad - \int_{\theta_2}^{\theta_1} G_{21}(\vec{r}, F(\theta'), \theta') J(\theta') d\theta', & y > -a \end{cases} \quad (4)$$

[case2] if $a < 0$ ($\theta_1 < \theta_2$), as shown in Fig. 1(b)

$$E^S(\vec{r}) = \begin{cases} E_1^S(\vec{r}) = - \int_{\theta_1}^{\theta_2} G_{12}(\vec{r}, F(\theta'), \theta') J(\theta') d\theta' \\ \quad - \int_{2\pi-\theta_1}^{\theta_2} G_{11}(\vec{r}, F(\theta'), \theta') J(\theta') d\theta', & y \leq -a \\ E_2^S(\vec{r}) = - \int_{\theta_1}^{\theta_2} G_{22}(\vec{r}, F(\theta'), \theta') J(\theta') d\theta' \\ \quad - \int_{2\pi-\theta_1}^{\theta_2} G_{21}(\vec{r}, F(\theta'), \theta') J(\theta') d\theta', & y > -a \end{cases} \quad (5)$$

with

$$J(\theta) = -j\omega\mu_0 \sqrt{F^2(\theta) + F'^2(\theta)} J_s(\theta)$$

Here $J_s(\theta)$ is the induced surface current density which is proportional to the normal derivative of electric field on the conductor surface. Note that G_1 and G_2 denote the Green's function for the line source in the Regions 1 and 2, respectively. $H_0^{(2)}$ is the Hankel function of the second kind of order zero. The boundary condition requires that the total tangential electric field on the surface of the scatterer must be zero and this yields an integral equation for $J(\theta)$. $J_s(\theta)$ is the induced surface current density, which is proportional to the normal derivative of the electric field on the conductor surface. For a conducting scatterer with non-uniform conductivity profile, the electromagnetic wave is able to penetrate into the interior of a scatterer, so the total tangential electric field at the surface of the scatterer is not equal to zero. The boundary condition for this case can be approximated by assuming that the total tangential electric field on the scatterer surface is related to surface current density through a surface impedance $Z_s(\omega, \theta)$:

$$\hat{n} \times \vec{E} = \hat{n} \times (Z_s \vec{J}_s) \quad (6)$$

where \hat{n} is the outward unit vector normal to the surface of the scatterer. The scatterer of interest here is a non-magnetic ($\mu = \mu_0$), imperfectly conducting cylinder with minimum radius of curvature a . The

surface impedance is expressed as $Z_s(\omega, \theta) \cong \sqrt{j\omega\mu_0/\sigma(\theta)}$. This approximation is valid as long as $|\text{Im}(N_c)ka| \gg 1$ and $\sigma \gg \omega\epsilon_0$, where “Im” means taking the imaginary part, and N_c is the complex refraction index of the conductor, given by $N_c = \sqrt{1 + \frac{\sigma(\theta)}{j\omega\epsilon_0}}$. The boundary condition at the surface of the scatterer given by Eq. (6) then can be applied to yield an integral equation for $J(\theta)$ as follows:

[case1] if $a > 0$ ($\theta_1 > \theta_2$), as shown in Fig. 1(a)

$$E_1^i(\vec{r}) = \int_{\theta_1-2\pi}^{\theta_2} G_{12}(\vec{r}, F(\theta'), \theta')J(\theta')d\theta' + \int_{\theta_2}^{\theta_1} G_{11}(\vec{r}, F(\theta'), \theta')J(\theta')d\theta' + j\sqrt{\frac{j}{\omega\mu_0\sigma(\theta)}} \frac{J(\theta)}{\sqrt{F^2(\theta) + F'^2(\theta)}}, \quad y \leq -a \tag{7}$$

$$E_2^i(\vec{r}) = \int_{\theta_1-2\pi}^{\theta_2} G_{22}(\vec{r}, F(\theta'), \theta')J(\theta')d\theta' + \int_{\theta_2}^{\theta_1} G_{21}(\vec{r}, F(\theta'), \theta')J(\theta')d\theta' + j\sqrt{\frac{j}{\omega\mu_0\sigma(\theta)}} \frac{J(\theta)}{\sqrt{F^2(\theta) + F'^2(\theta)}}, \quad y > -a$$

[case2] if $a < 0$ ($\theta_1 < \theta_2$), as shown in Fig. 1(b)

$$E_1^i(\vec{r}) = \int_{\theta_1}^{\theta_2} G_{12}(\vec{r}, F(\theta'), \theta')J(\theta')d\theta' + \int_{\theta_2}^{2\pi-\theta_1} G_{11}(\vec{r}, F(\theta'), \theta')J(\theta')d\theta' + j\sqrt{\frac{j}{\omega\mu_0\sigma(\theta)}} \frac{J(\theta)}{\sqrt{F^2(\theta) + F'^2(\theta)}}, \quad y \leq -a \tag{8}$$

$$E_2^i(\vec{r}) = \int_{\theta_1}^{\theta_2} G_{22}(\vec{r}, F(\theta'), \theta')J(\theta')d\theta' + \int_{\theta_2}^{2\pi-\theta_1} G_{21}(\vec{r}, F(\theta'), \theta')J(\theta')d\theta' + j\sqrt{\frac{j}{\omega\mu_0\sigma(\theta)}} \frac{J(\theta)}{\sqrt{F^2(\theta) + F'^2(\theta)}}, \quad y > -a$$

For the direct scattering problem, the scattered field E^S is calculated by assuming that the shape is known. This can be achieved by first solving J in Eqs (7) and (8) and then calculating E^S in Eqs (4) and (5) for the cases 1 and 2, respectively. For the inverse scattering problem, we assume the approximate center of the scatterer is known, then, the shape function $F(\theta)$ and conductivity profile $\sigma(\theta)$ can be expanded as:

$$F(\theta) = \sum_{n=0}^{N/2} B_n \cos(n\theta) + \sum_{n=1}^{N/2} C_n \sin(n\theta) \tag{9}$$

$$\sigma(\theta) = \sum_{n=0}^{N/2} D_n \cos(n\theta) + \sum_{n=1}^{N/2} E_n \sin(n\theta) \tag{10}$$

where B_n , C_n , D_n and E_n are all real numbers to be determined, and $2(N + 1)$ is the total number of unknowns for the shape function and conductivity profile. Note that the discretisation number of $J(\theta)$ for the inverse problem must be different from that for the direct problem, since it is crucial that the synthetic data generated through a direct solver are not like those obtained by the inverse solver. In our simulation, the discretisation number for the direct problem is twice as many as that for the inverse problem.

The parameters B_n , C_n , D_n and E_n are coded using Gray code [20], and the processes of reproduction, mutation and crossover of SSGA are employed to optimize B_n , C_n , D_n and E_n . Here, we use an improved SSGA for our imaging problem. More details of the improved efficient SSGA are addressed in next section.

3. Efficient steady state genetic algorithm

Genetic algorithms belong to the global optimization method and are based on the idea of genetic recombination and evaluation in nature [41]. In a traditional GA, each reproduction cycle can produce up to the entirely new generation of children, which then replaces the parent generation. But in the steady state GA (SSGA), it only has a portion of the current generation to be replaced by children generated in the reproductive cycle, resulting in overlapping generations. The temporary population of children is inserted into the original parent population, by replacing certain selected individuals in the parent population. As a variant to the traditional GA, SSGA is to insert the temporary population into the parent population, producing a temporarily expanded parent population. Individuals are selected and deleted from the expanded population until the original population size is reached again. The key distinction between an SSGA and a traditional GA is on the number of fitness calculation. In a traditional GA, it uses the high crossover rate and mutation rate to generate nearly all the population in each new generation. On the contrary, SSGA only need to generate a small portion of population in each new generation [20]. In other words, the number of fitness calculation corresponding to the new generation is large in a traditional GA compared with SSGA. Note that most CPU time consumed in the simulation is contributed from the calculation of the fitness value. As a result, SSGA is very suitable for inverse problem in regard of reducing the number of fitness calculation.

The SSGA starts with a population containing a total of N_p candidates (i.e., N_p is the population size). Each candidate is described by a chromosome. The initial population can simply be created by taking N_p random chromosomes. Then, the SSGA iteratively generates a new population, which is derived from the previous population through the application of the reproduction, crossover, and mutation operators. During the course, the SSGA is used to maximize the following objective function:

$$GOF = \left\{ \frac{1}{M_t} \sum_{m=1}^{M_t} \left| E_s^{\text{exp}}(\bar{r}_m) - E_s^{\text{cal}}(\bar{r}_m) \right|^2 / |E_s^{\text{exp}}(\bar{r}_m)|^2 + \alpha \left[\|F'(\theta)\|^2 \right] \right\}^{-1/2} \quad (11)$$

where M_t is the total number of the measurements. $E_s^{\text{exp}}(\vec{r})$ and $E_s^{\text{cal}}(\vec{r})$ are the measured scattered field and the calculated scattered field, respectively. The factor $\alpha \|F'(\theta)\|^2$ can be interpreted as certain extra smoothness requirement for the boundary $F(\theta)$. The optimal value of α is mostly dependent on the dimensions of the geometry. One can always choose an enough large value to ensure the convergence, although overestimation will result in a very smooth reconstruction.

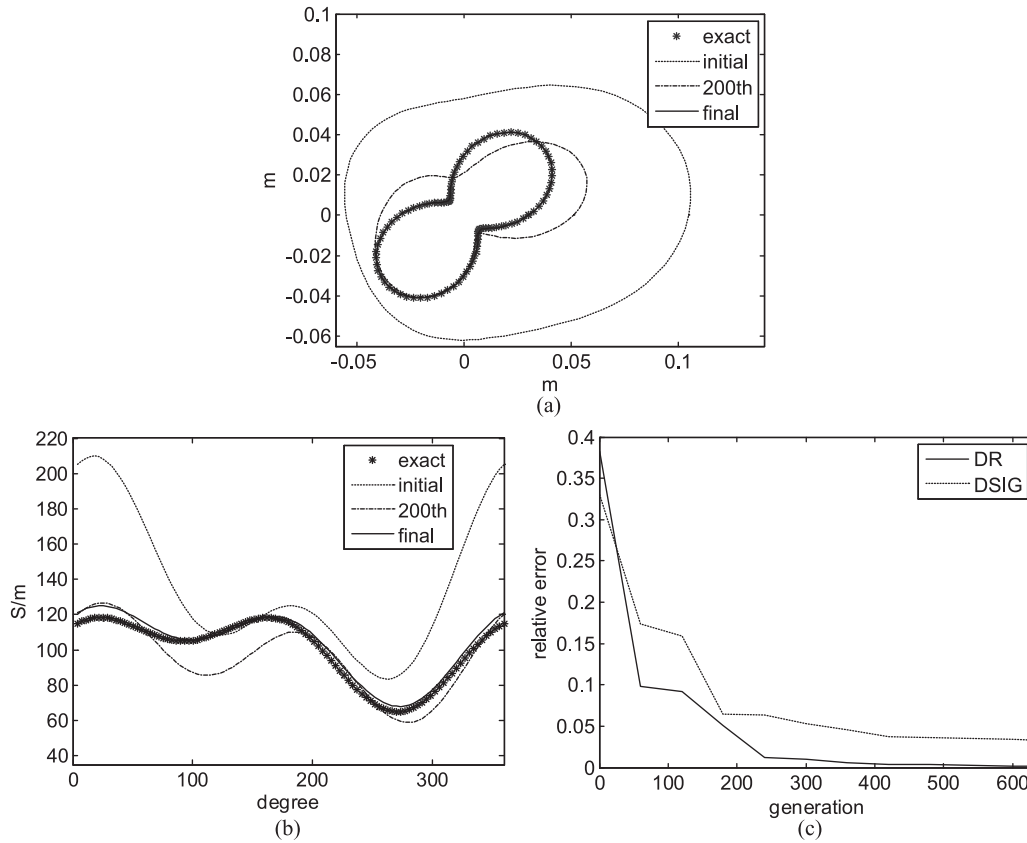


Fig. 2. (a) Shape function for example 1. The star curve represents the exact shape, while the solid curves are calculated shape during iteration process. (b) Conductivity function for example 1. The star curve represents the exact conductivities, while the solid curves are the calculated conductivities during iteration process. (c) The errors of shape and conductivity function versus generation.

4. Numerical results

In this section, we report some numerical results obtained by computer simulations using the method described in the Section 2.

Let us consider a conducting cylinder with non-uniform conducting profile which is partially immersed in a lossless half-space ($\sigma_1 = \sigma_2 = 0$) and the parameter a is set to zero. In order to simulate sandy soil environment [42], the permittivity in Regions 1 and 2 is characterized by $\varepsilon_1 = \varepsilon_0$ and $\varepsilon_2 = 2.7\varepsilon_0$, respectively. The frequency of the incident wave is chosen to be 1 GHz, with incident angles ϕ_1 equal to 45° and 315° , respectively. For each incident wave 8 measurements are made at the points equally separated on a semi-circle with the radius of 3 m in Region 1. Therefore, there are totally 16 measurements in each simulation. The number of unknowns is set to be 18 (i.e., $2(N + 1) = 18$), for the sake of the computation time. The population size of 100 is chosen and rank selection scheme is used with the top 30 individuals being reproduced accords to the rank. The search range for the unknown coefficient of the shape function is chosen to be from 0 to 0.1 and the unknown coefficient of the conductivity is chosen to be from 1 to 200 S/m. The extreme values of the coefficient of the shape function can be determined by the prior knowledge of the object. The crossover rate is set to 0.1 such that only

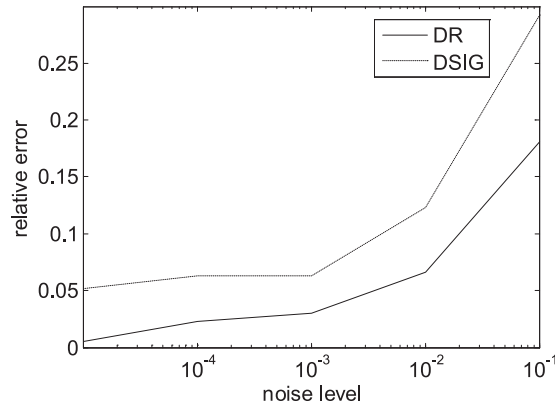


Fig. 3. Relative errors of shape and conductivity as a function of noise.

10 iterations are performed per generation. The mutation probability is set to 0.05 and the value of α in Eq. (11) is set to be 0.001. In the following examples, the size of scatter is about one wavelength, so the frequency is in the resonance range.

For the first example, the shape function and conductivity profile are chosen to be $F(\theta) = (0.03 + 0.02 \sin 2\theta)$ m and $\sigma(\theta) = (100 + 15 \cos 2\theta + 20 \sin \theta)$ S/m. The reconstructed shape function and conductivity profile for the best population member are plotted in Figs 2(a) and (b). The errors for the reconstructed shape DR and the reconstructed conductivity profile DSIG are shown in Fig. 2(c), of which DR and DSIG are defined as

$$DR = \left\{ \frac{1}{N'} \sum_{i=1}^{N'} \left[F^{cal}(\theta_i) - F(\theta_i) \right]^2 / F^2(\theta_i) \right\}^{1/2} \quad (12)$$

$$DSIG = \left\{ \frac{1}{N'} \sum_{i=1}^{N'} \left[\sigma^{cal}(\theta_i) - \sigma(\theta_i) \right]^2 / \sigma^2(\theta_i) \right\}^{1/2} \quad (13)$$

where N' is set to 100. The quantities DR and $DSIG$ provide measures of how well $F^{cal}(\theta)$ approximates $F(\theta)$ and $\sigma^{cal}(\theta)$ approximates $\sigma(\theta)$, respectively. From Figs 2(a)~(c), it is clear that the reconstruction of the shape and the conductivity profile are quite good. In addition, we also see that the reconstruction of conductivity profile does not change rapidly toward the exact value until DR is small enough. This can be explained by the fact that the shape function makes a stronger contribution to the scattered field than the conductivity does. In other words, the reconstruction of the shape function has a higher priority than the reconstruction of the conductivity profile. To investigate the sensitivity of the imaging algorithm against random noise, two independent Gaussian noises with zero mean have been added to the real and imaginary parts of the simulated scattered fields. Normalized standard deviations of 10^{-5} , 10^{-4} , 10^{-3} , 10^{-2} and 10^{-1} are used in the simulations. The normalized standard deviation mentioned earlier is defined as the standard deviation of the Gaussian noise divided by the rms value of the scattered fields. Here, the signal-to-noise ratio (SNR) is inversely proportional to the normalized standard deviation. The numerical result for this example is plotted in Fig. 3. It is observed that the effect of noise is negligible for normalized standard deviations below 10^{-3} .

In the second example, we test the following shape function $F(\theta) = (0.025 + 0.015 \cos 3\theta + 0.005 \sin \theta)$ m and conductivity profile $\sigma(\theta) = (75 + 10 \sin \theta + 25 \sin 3\theta)$ S/m. The purpose of this

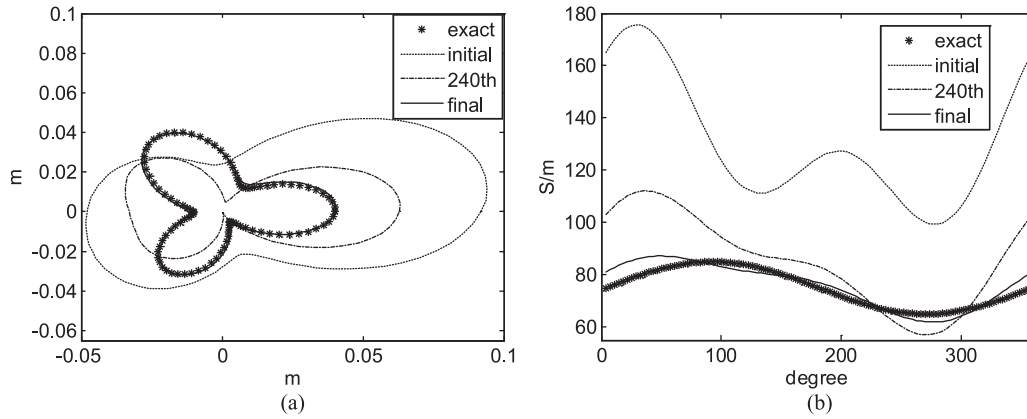


Fig. 4. (a) Shape function for example 2. The star curve represents the exact shape, while the solid curves are the calculated shape during iteration process. (b) Conductivity function for example 2. The star curve represents the exact conductivity, while the solid curves are the calculated conductivities during iteration process.

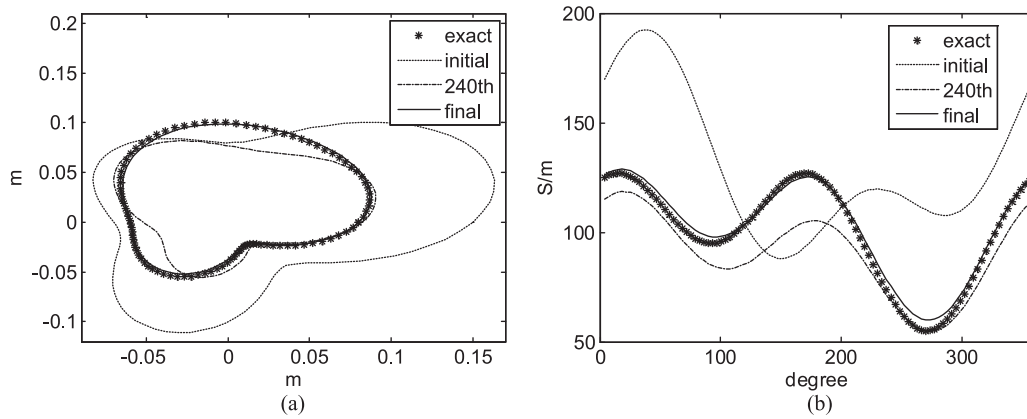


Fig. 5. (a) Shape function for example 3. The star curve represents the exact shape, while the solid curves are calculated shape during iteration process. (b) Conductivity profile for example 3. The star curve represents the exact conductivity, while the solid curves are the calculated conductivities during iteration process.

example is to show that the proposed method is able to reconstruct different shape and conductivity profile. Satisfactory results are shown in Figs 4(a) and (b).

In the third example, the shape function and conductivity profile are selected to be $F(\theta) = (0.07 + 0.03 \sin \theta + 0.01 \sin 2\theta + 0.01 \cos 3\theta) m$ and $\sigma(\theta) = (100 + 25 \cos 2\theta + 20 \sin \theta + 15 \sin 3\theta) S/m$. Note that the shape function is not symmetrical about either x axis and y axis. This example has further verified the reliability of the proposed algorithm. Refer to Figs 5(a) and (b) for details.

5. Conclusions

We have presented a study of applying the SSGA to reconstruct the shape and conductivity profile of a partially immersed metallic object through the measured scattered E fields. Based on an integral equation, the microwave imaging problem is recast as a nonlinear optimization one. Then an objective

function is defined in term of the difference between the measured scattered electric fields and the calculated scattered fields such that the shape and the conductivity profile of the conductor can be estimated by using SSGA. The results show that even when the initial guess is far from the exact one, good reconstruction can be achieved from the measured scattered fields both with and without the additive Gaussian noise. Numerical results also illustrate that the conductivity reconstruction is more sensitive to noise than the shape reconstruction is.

Acknowledgment

This work was supported by National Science Council, Republic of China, under Grant NSC-97-2221-E-237-006.

References

- [1] C.H. Sun, C.L. Li, C.C. Chiu and C.H. Huang, Time domain image reconstruction for a buried 2D homogeneous dielectric cylinder using NU-SSGA, *Research in Nondestructive Evaluation* **22**(1) (Jan 2011), 115.
- [2] C.H. Chen, C.C. Chiu, C.H. Sun and W.L. Chang, Two-dimensional finite-difference time domain inverse scattering scheme for a perfectly conducting cylinder, *Journal of Applied Remote Sensing* **5** (May 2011), 053522.
- [3] M.R. Hajihashem and M.E. Shenawee, Level set algorithm for shape reconstruction of non-overlapping three-dimensional penetrable targets, *IEEE Transactions Geoscience and Remote Sensing* **50**(1) (Jan 2012), 75–86.
- [4] C.H. Sun, C.C. Chiu and C.J. Lin, Image reconstruction of inhomogeneous biaxial dielectric cylinders buried in a slab medium, *International Journal of Applied Electromagnetics and Mechanics* **34**(1–2) (Nov 2010), 33–48.
- [5] C.C. Chiu, C.H. Sun and Y.S. Fan, Shape reconstruction of 2-D perfectly conducting cylinder targets using the particle swarm optimization, *Imaging Science Journal* **60**(2) (Apr 2012), 83–89.
- [6] H. Ammari, H. Kang, H. Lee and W.K. Park, Asymptotic imaging of perfectly conducting cracks, *SIAM Journal on Scientific Computing* (2010), 894–922.
- [7] T.G. Papadopoulos and I.T. Rekanos, Time-domain microwave imaging of inhomogeneous Debye dispersive scatterers, *IEEE Transactions on Antennas and Propagation* **60**(2) (Feb 2012), 1197–1202.
- [8] M. El-Shenawee, O. Dorn and M. Moscoso, An adjoint-field technique for shape reconstruction of 3-D penetrable object immersed in lossy medium, *IEEE Trans Antennas Propag* **57**(2) (Feb 2009), 520–534.
- [9] M. Benedetti, D. Lesselier, M. Lambert and A. Massa, Multiple-shape reconstruction by means of multiregion level sets, *IEEE Transactions Geoscience and Remote Sensing* **48**(5) (May 2010), 2330–2342.
- [10] T.G. Papadopoulos and I.T. Rekanos, Estimation of the parameters of Lorentz dispersive media using a time-domain inverse scattering technique, *IEEE Transactions on Magnetics* **48**(2) (Feb 2012), 219–222.
- [11] I. Catapano, L. Crocco and T. Isernia, Improved sampling methods for shape reconstruction of 3-D buried targets, *IEEE Transactions on Geoscience and Remote Sensing* **46**(10) (Oct 2008), 3265–3273.
- [12] P.C. Sabatier, Theoretical considerations for inverse scattering, *Radio Science* **18** (Jan 1983), 1–18.
- [13] C.C. Chiu and Y.W. Kiang, Electromagnetic imaging for an imperfectly conducting cylinder, *IEEE Transactions on Microwave Theory and Techniques* **39** (Sept 1991), 1632–1639.
- [14] C.C. Chiu and Y.W. Kiang, Electromagnetic inverse scattering of a conducting cylinder buried in a lossy half-space, *IEEE Transactions on Antennas and Propagation* **40** (Dec 1992), 1562–1565.
- [15] D. Colton and P. Monk, A novel method for solving the inverse scattering problem for time-harmonic acoustic waves in the resonance region II, *SIAM J Appl Math* **46** (Jun 1986), 506–523.
- [16] A. Kirsch, R. Kress, P. Monk and A. Zinn, Two methods for solving the inverse acoustic scattering problem, *Inverse Problems* **4** (Aug 1998), 749–770.
- [17] R.E. Kleinman and P.M. van den Berg, Two-dimensional location and shape reconstruction, *Radio Sci* **29** (Jul–Aug 1994), 1157–1169.
- [18] T. Moriyama, Z. Meng and T. Takenaka, Forward-backward time-stepping method combined with genetic algorithm applied to breast cancer detection, *Microwave and Optical Technology Letters* **53**(2) (2011), 438–442.
- [19] W. Chien, Inverse scattering of an un-uniform conductivity scatterer buried in a three-layer structure, *Progress In Electromagnetic Research PIER* **82** (2008), 1–18.
- [20] W. Chien and C.-C. Chiu, Using NU-SSGA to reduce the searching time in inverse problem of a buried metallic object, *IEEE Transactions on Antennas and Propagation* **53**(10) (October 2005), 3128–3134.

- [21] M. Benedetti, M. Donelli and A. Massa, Multicrack detection in two-dimensional structures by means of ga-based strategies, *IEEE Transaction on Antennas and Propagation* **55**(1) (Jan 2007), 205–215.
- [22] M. Benedetti, G. Franceschini, R. Azaro and A. Massa, A numerical assessment of the reconstruction effectiveness of the integrated GA-based multicrack strategy, *IEEE Antennas and Wireless Propagation Letters* **6** (2007), 271–274.
- [23] W. Chien, C.H. Huang, C.C. Chiu and C.L. Li, Image reconstruction for 2D homogeneous dielectric cylinder using FDTD method and SSGA, *International Journal of Applied Electromagnetics and Mechanics* **32**(2) (Feb 2010), 111–123.
- [24] W. Chien, C.H. Huang and C.C. Chiu, Cubic-spline expansion for a two-dimensional periodic conductor in free space, *International Journal of Applied Electromagnetics and Mechanics* **24**(1–2) (Nov 2006).
- [25] W. Chien, C.C. Chiu and C.L. Li, Cubic-spline expansion with GA for a conducting cylinder buried in a slab medium, *Electromagnetics* **26**(5) (July 2006), 329–343.
- [26] C.H. Sun, C.L. Liu, K.C. Chen, C.C. Chiu, C.L. Li and C.C. Tasi, Electromagnetic transverse electric wave inverse scattering of a partially immersed conductor by steady-state genetic algorithm, *Electromagnetics* **28**(6) (Aug 2008), 389–400.
- [27] W. Chien, C.H. Sun and C.C. Chiu, Image reconstruction for a partially immersed imperfectly conducting cylinder by genetic algorithm, *International Journal of Imaging Systems and Technology* **19** (Dec 2009), 299–305.
- [28] C.H. Sun, C.C. Chiu and C.L. Li, Time-domain inverse scattering of a two-dimensional metallic cylinder in slab medium using asynchronous particle swarm optimization, *Progress In Electromagnetic Research M PIER M* **14** (Aug 2010), 85–100.
- [29] C.C. Chiu, C.H. Sun and W.L. Chang, Comparison of particle swarm optimization and asynchronous particle swarm optimization for inverse scattering of a two-dimensional perfectly conducting cylinder, *International Journal of Applied Electromagnetics and Mechanics* **35**(4) (Apr 2011), 249–261.
- [30] C.L. Li, C.C. Chiu and C.H. Huang, Time domain inverse scattering for a homogenous dielectric cylinder by asynchronous particle swarm optimization, *Journal of Testing and Evaluation* **38**(3) (May 2011), 102–868.
- [31] M. Donelli, G. Franceschini, A. Martini and A. Massa, An integrated multiscaling strategy based on a particle swarm algorithm for inverse scattering problems, *IEEE Transactions on Geoscience and Remote Sensing* **44**(2) (Feb 2006), 298–312.
- [32] I.T. Rekanos, Shape reconstruction of a perfectly conducting scatterer using differential evolution and particle swarm optimization, *IEEE Transactions on Geoscience and Remote Sensing* **46**(7) (Jul 2008), 1967–1974.
- [33] C.C. Chiu and W.C. Hsiao, Comparison of asynchronous particle swarm optimization and dynamic differential evolution for partially immersed conductor, *Waves in Random and Complex Media* **21**(3) (Aug 2011), 485–500.
- [34] C.H. Sun, C.C. Chiu, W. Chien and C.L. Li, Application of FDTD and dynamic differential evolution for inverse scattering of a two-dimensional perfectly conducting cylinder in slab medium, *Journal of Electronic Imaging* **19** (Dec 2010), 043016.
- [35] C.H. Sun, C.C. Chiu, C.L. Li and C.H. Huang, Time domain image reconstruction for homogenous dielectric objects by dynamic differential evolution, *Electromagnetics* **30**(4) (May 2010), 309–323.
- [36] A. Qing, Dynamic differential evolution strategy and applications in electromagnetic inverse scattering problems, *IEEE Transactions on Geoscience and Remote Sensing* **44**(1) (Jan 2006), 116–125.
- [37] A. Semnani, I.T. Rekanos, M. Kamyab and T.G. Papadopoulos, Two-dimensional microwave imaging based on hybrid scatterer representation and differential evolution, *IEEE Trans Antennas Propag* **58**(10) (Oct 2010), 3289–3298.
- [38] C.L. Li, W. Chien, C.H. Huang and C.C. Chiu, Time domain microwave imaging for a buried dielectric cylinder by dynamic differential evolution, *International Journal of Applied Electromagnetics and Mechanics* **34**(1–2) (Nov 2010), 73–86.
- [39] C.H. Sun and C.C. Chiu, Electromagnetic imaging of buried perfectly conducting cylinders targets using the dynamic differential evolution, *International Journal of RF and Microwave Computer-Aided Engineering* **22**(2) (Mar 2012), 141–146.
- [40] C.C. Chiu and W.T. Chen, Electromagnetic imaging for an imperfectly conducting cylinder by the genetic algorithm, *IEEE Trans. Microwave Theory and Tec* **48** (Nov 2000), 1901–1905.
- [41] D.E. Goldberg, *Genetic Algorithm in Search, Optimization and Machine Learning*, Addison-Wesley, 1989.
- [42] B. Sai and P. van Genderen, On the design of the UWB front-end of GPR for landmine detection, *Proc International Conference on Radar Systems*, Brest, France, Session 1.7, May 17–21 1999, pp. 1–5.

Copyright of International Journal of Applied Electromagnetics & Mechanics is the property of IOS Press and its content may not be copied or emailed to multiple sites or posted to a listserv without the copyright holder's express written permission. However, users may print, download, or email articles for individual use.